Magnetic compensation of gravity forces in (p-) hydrogen near its critical point: Application to weightless conditions

R. Wunenburger,[1] D. Chatain,[2] Y. Garrabos,[1] and D. Beysens[2]
[1]*ESEME, Institut de Chimie de la Matière Condensée de Bordeaux, UPR 9048, Centre National de la Recherche Scientifique, Université Bordeaux I, Avenue Dr. A. Schweitzer, F-33608 Pessac Cedex, France*
[2]*ESEME, Service des Basses Températures, DRFMC, CEA-Grenoble, 17 rue des Martyrs, F-38054 Grenoble Cedex 09, France*
(Received 28 October 1999)

We report a study concerning the compensation of gravity forces in two-phase (p-) hydrogen. The sample is placed near one end of the vertical z axis of a superconducting coil, where there is a near-uniform magnetic field gradient. A variable effective gravity level g can thus be applied to the two-phase fluid system. The vanishing behavior of the capillary length ℓ_C at the critical point is compensated by a decrease in g and ℓ_C is kept much smaller than the cell dimension. For g ranging from 1 to 0.25 times Earth's gravity (modulus g_0) we compare the actual shape of the meniscus to the expected shape in a homogeneous gravity field. We determine ℓ_C in a wide range of reduced temperature $\tau=(T_C-T)/T_C=[10^{-4}-0.02]$ from a fit of the meniscus shape. The data are in agreement with previous measurements further from T_C performed in n-H_2 under Earth's gravity. The effective gravity is homogeneous within $10^{-2}g_0$ for a 3 mm diameter and 2 mm thickness sample and is in good agreement with the computed one, validating the use of the apparatus as a variable gravity facility. In the vicinity of the levitation point (where magnetic forces exactly compensate Earth's gravity), the computed axial component of the acceleration is found to be quadratic in z, whereas its radial component is proportional to the distance to the axis, which explains the gas-liquid patterns observed near the critical point.

PACS number(s): 68.10.−m, 64.60.Fr, 07.20.Mc

I. INTRODUCTION

Magnetic levitation of matter consists of the compensation of its weight by magnetic forces. Because of the weak diamagnetic susceptibility of many nonmagnetic substances, strong magnetic fields are needed for magnetic levitation. Such field intensities have been attained only recently. Since the first demonstration of magnetic levitation of diamagnetic substances [1,2], this technique has chiefly been applied to the containerless handling of liquids, solids, or living bodies [1–7], the simulation of low gravity or weightless conditions for life science [3], and fluid physics (noncoalescence of liquid drops in contact [5,6], deformations modes of drops [7], investigation of the lambda transition in helium [8]). In some previous work using magnetic weightlessness, precise measurements of the magnetic field [8] as well as detailed analytical and numerical calculations of the force field applied to the sample were performed [1,4,6,8]. However, no measurement of the residual gravity has been performed. In this paper, we present a simple method to check the homogeneity of the total acceleration field. It is based on the analysis of the shape of the gas-liquid interface and on the vanishing behavior of the capillary length of a liquid-gas mixture of hydrogen in equilibrium near its critical point.

Containerless handling applications require only a global compensation of the total weight of the body and a stable levitation to be met, whereas gravity compensation needs more conditions to be fulfilled. Indeed, when a diamagnetic sample is placed in a magnetic field $\mathbf{B}$, each of its molecules is subjected to a force that is proportional to its magnetic susceptibility χ and to the local gradient of $\mathbf{B}^2$. The resulting magnetic acceleration vector $\mathbf{a}_m$ induced by the magnetic field $\mathbf{B}$ is

$$\mathbf{a}_m=\frac{\chi}{\mu_0\rho}\boldsymbol{\nabla}\left(\tfrac{1}{2}\mathbf{B}^2\right), \tag{1}$$

where ρ is the sample density and $\mu_0=4\pi\times10^{-7}\,\mathrm{H\,m^{-1}}$. The total acceleration vector applied to the sample on the Earth is

$$\mathbf{g}=\mathbf{g}_0+\mathbf{a}_m, \tag{2}$$

where $\mathbf{g}_0$ is the gravitational acceleration vector. Let g^* be the reduced acceleration modulus (effective gravity level)

$$g^*=\frac{\|\mathbf{g}\|}{\|\mathbf{g}_0\|}, \tag{3}$$

which can be larger or smaller than 1 due to the vectorial character of Eq. (2). The acceleration field $\mathbf{g}$ is homogeneous at the length scale of the sample provided that the $\mathbf{B}^2$ gradient and the chemical composition of the sample are homogeneous at the sample length scale. Under these conditions, Earth's gravitational acceleration can be increased, partially compensated, or exactly cancelled in the same manner at each point of the sample. This leads to the accomplishment of a tunable artificial gravity, ranging from large to low values of g^*, and ultimately reaching weightlessness ($g^*=0$).

Since a homogeneous acceleration field can be achieved only within a given precision, it is useful to evaluate the maximum deviation of g^* from its mean value within the sample

$$\Delta g^*=\max_{\text{sample}}\left(\left|\langle g^*\rangle_{\text{sample}}-g^*\right|\right). \tag{4}$$

When global compensation of weight is achieved (levitation), Δg^* is called the ''residual gravity.'' It is a quantitative evaluation of the ''quality'' of weightlessness and allows the various low gravity facilities (magnetic levitation, parabolic flights, sounding rockets, orbital platforms, etc.) to be compared.

During the last decade, experimental investigation of the physics of pure fluids near their critical point has benefited from weightless conditions, which prevent convection and stratification. (For a review, see Ref. [9].) Pure fluids exhibit universal behavior near their critical point. This means that some of their thermophysical properties diverge (e.g., the specific heat) or vanish (e.g., the thermal diffusivity) at the critical point, in a scaled way valid for all fluids, depending only on the reduced distance to the critical point $\tau=|T_C-T|/T_C$ (T is the temperature of the fluid, and T_C is its critical temperature). This universal behavior allows a large variety of phenomena to be studied in any pure fluid by changing its temperature. We developed a magnetic levitation apparatus dedicated to para-hydrogen (p-H_2). p-H_2 was chosen because of its high magnetic susceptibility ($\chi/\rho=-2.51\times10^{-8}\ \mathrm{m^3\,kg^{-1}}$) and its low critical temperature value ($T_C=33\ \mathrm{K}$). This apparatus can also be regarded more generally as a variable effective gravity facility that allows the effect of gravity to be studied in fluid physics. It presently allows a variable acceleration to be imposed to a hydrogen sample in a range running from levitation ($g^*=0$) to $g^*=2.2$. In particular, the Moon and Mars gravity ($g^*\approx\frac{1}{6}$ and $\frac{1}{3}$) can be easily reproduced.

We now present the physical grounds of the method that allow us to check the homogeneity of the acceleration field. A two-phase gas-liquid sample in thermodynamic equilibrium is characterized by its interfacial tension σ. When only interfacial forces act, the bubble has a spherical shape, which minimizes its interfacial energy. When it is submitted to an acceleration field **g**, it is deformed so as to minimize the sum of its potential and interfacial energies. The amplitude of this deformation is an increasing function of the Bond number $\mathcal{B}$ defined as the ratio between the interfacial energy and the potential energy:

$$\mathcal{B}=\frac{(\rho_L-\rho_V)gl^2}{\sigma}=\frac{l^2}{\ell_C^2}, \tag{5}$$

where l is the diameter of the bubble, $\rho_L(\rho_V)$ the density of the liquid (gas) phase, and ℓ_C the capillary length, defined as

$$\ell_C=\sqrt{\sigma/g(\rho_L-\rho_V)}=\frac{1}{\sqrt{g^*}}\sqrt{\sigma/g_0(\rho_L-\rho_V)}. \tag{6}$$

ℓ_C is the length scale of the resulting deformations of the bubble due to gravity. The shape of the interface gives information about the intensity of the acceleration field when $\mathcal{B}>1$, i.e., when the capillary length is smaller than the size of the bubble.

The critical point is the end point of the liquid-gas coexistence curve of a pure fluid in the P-T diagram (P is pressure). At the critical point there is no difference between the two phases and the interface disappears. Near the critical point and along the coexistence curve the reduced difference between the densities of the two phases varies as

$$\frac{\rho_L-\rho_V}{\rho_C}=2B_0\tau^{0.325}, \tag{7}$$

where ρ_C is the critical density. The amplitude B_0 is a system-dependent parameter ($B_0=1.61$) and 0.325 is the value of the universal critical exponent [11]. The surface tension σ between the two phases also vanishes at the critical point as

$$\sigma=\sigma_0\tau^{1.26}. \tag{8}$$

The amplitude σ_0 depends on the fluid ($\sigma=5.4\times10^{-3}\ \mathrm{N\,m^{-1}}$ for $n-H_2$) and 1.26 is the value of the universal critical exponent. According to Eq. (6), the capillary length ℓ_C vanishes at the critical point as

$$\ell_C=\frac{1}{\sqrt{g^*}}\ell_{C0}\tau^{0.4675},\quad \ell_{C0}=\sqrt{\sigma_0/2B_0g_0\rho_C}. \tag{9}$$

For n-hydrogen $\ell_{C0}=2.39\ \mathrm{mm}$ [12]. When g^* goes to zero, the capillary length may diverge at constant temperature. However, if the critical point is simultaneously approached, ℓ_C also goes to zero at constant g^*. Going closer to the critical point as the acceleration field is lowered allows the condition $\mathcal{B}>1$ to be maintained, i.e., information about the acceleration field can still be extracted from the shape of the interface. The key point of this method is that the low intensity of the acceleration field is compensated by the fact that the near-critical interface becomes very deformable. This makes this two-phase system very sensitive to the remaining accelerations as demonstrated in the following.

The paper is organized as follows. In Sec. II the experimental apparatus is presented in detail. In Sec. III a method to check the homogeneity of the acceleration field and to deduce the capillary length and the acceleration field from the shape of the gas-liquid interface is described. In Sec. IV a computation of the residual acceleration field in the levitated state is proposed and compared to the experimental gas-liquid patterns.

II. EXPERIMENTAL PROCEDURE

The apparatus consists of two parts, the cryostat containing the superconducting coil and the anticryostat containing the sample and the optics. It is schematically shown in Fig. 1. The axis of the coil is vertical. The cryostat is composed of two stages. A Dewar containing liquid N_2 surrounds another Dewar containing liquid He maintained at 2.17 K with the help of a heat exchanger. A superconductive coil of total height 200 mm is immersed inside the helium bath. It supports a current up to 65 A and produces a magnetic field up to 10 T on its axis, which is parallel to Earth's gravity. The anticryostat is a cylindrical container partially immersed inside the helium bath, standing along the axis of the coil, in which vacuum (10^{-4} Pa) is maintained for thermal isolation purposes.

The cell containing the H_2 sample is positioned along the axis of the coil. The altitude of the sample cell center along the coil axis corresponds to the maximum of intensity of the upward magnetic force, at the upper end of the coil, i.e., at 85 mm from its center. On the coil axis, **g** is vertical and Eq. (2) reduces to $g=g_0-a_m$ at the upper end ($g=g_0+a_m$ at the lower end). Levitation is attained when the electric current in the coil I_E is equal to 63.1 A, corresponding to a magnetic

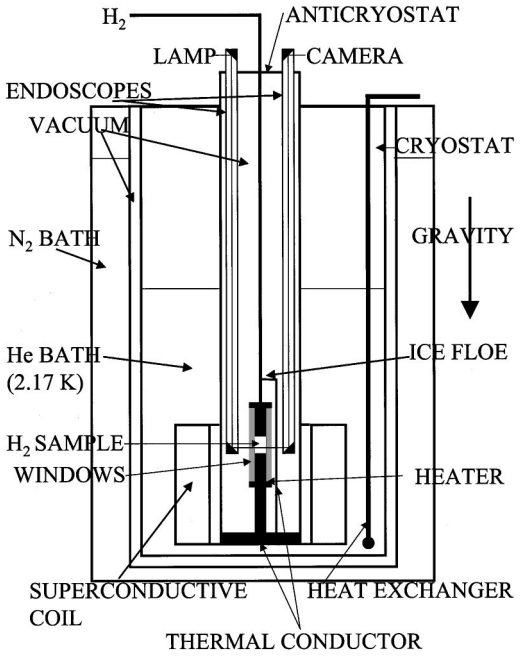

FIG. 1. Experimental setup (schematic representation).

field of magnitude 6.65 T in the cell. According to the linear relation between the electric current I_E in the coil and the magnetic field, g^* is computed using the relation

$$g^*(I_E)=g_0[1-(I_E/63.1)^2]. \tag{10}$$

The cell is made of electrolytic copper. The cavity containing the fluid is cylindrical (3 mm in diameter) with its axis horizontal (y axis), perpendicular to the coil axis. It is closed by two parallel sapphire windows 2 mm apart and sealed by indium rings. The cell is in thermal contact with the helium bath by means of a thermal conductor. Its temperature is measured with a Cernox thermometer and is controlled via an electrical resistance supplied by a closed loop temperature control device. The temperature control is ± 1 mK at 33 K and the working temperature range is 15–40 K. A power of 600 mW is needed to maintain the cell temperature at 33 K. The cell is filled with purified, pressurized H_2 at room temperature through a capillary. This capillary is closed by a H_2 ice floe, whose formation is locally allowed by a thermal conductor in contact with the helium bath (solidification temperature 14 K). The gas-liquid system is observed in light transmission. Parallel light is directed by means of mirrors from outside the anticryostat to the sample. The beam is parallel to the axis of the cylindrical cell and is directed by mirrors to the camera outside the anticryostat.

The cell is filled at critical density as checked by the position of the meniscus in the middle of the vessel at the critical temperature. When H_2 is cooled in the cell, the n-H_2 p-H_2 equilibrium is shifted and the percentage of p-H_2 increases from 25% at room temperature to 96% at 30 K [10]. The critical coordinates of n-H_2 (p-H_2) are $T_C=33.24\,\mathrm{K}$ (32.976 K), $P_C=1.298\,\mathrm{MPa}$ (1.2928 MPa), and $\rho_C=30.09\,\mathrm{kg\,m^{-3}}$ ($31.426\,\mathrm{kg\,m^{-3}}$) [10]. The slow conversion of n-H_2 to p-H_2 is followed in time by determining at regular time intervals the temperature at which the meniscus disappears (critical temperature of the ortho-para hydrogen mixture). We find that the critical temperature decays exponentially with a time constant of order 50 h. When the critical temperature has reached a constant value within ± 1 mK, equilibrium is supposed to be attained and the analysis of the meniscus shape starts.

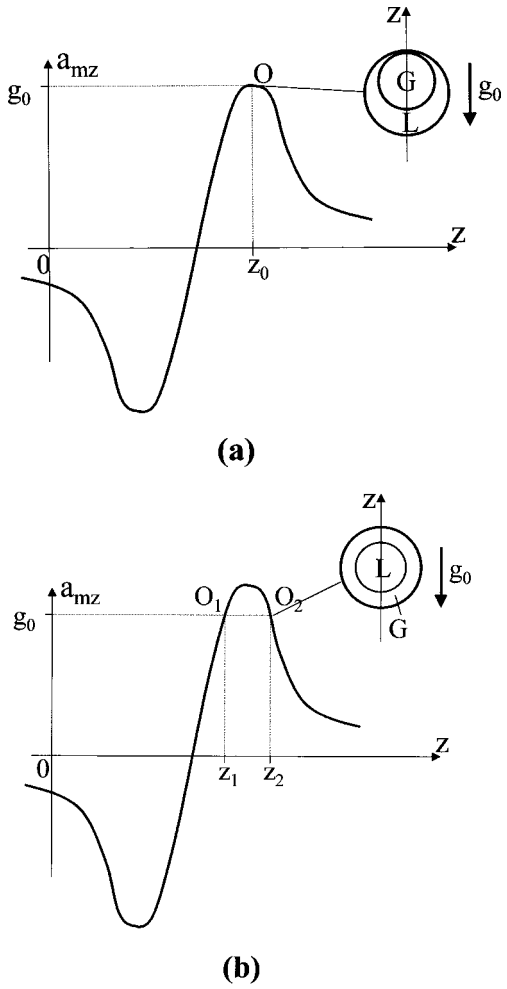

FIG. 2. Sketch of the variations of the axial magnetic acceleration $a_{mz}(z)$ along the vertical z axis in two different experimental configurations. Neither the radial acceleration inhomogeneities nor the consequences of the total wetting are taken into account in the schematic phase distribution inside the cell shown on the right-hand side of the graph. (a) Our setup: the sample cell is placed at the maximum (equal to g_0) of the magnetic acceleration. The resulting effective acceleration is quadratic in z, and the levitation is an unstable equilibrium. (b) Setup of Ref. [6]: the sample cell is placed at O_2 slightly above the maximum (slightly larger than g_0) of the magnetic acceleration. At points O_1 and O_2 $a_{mz}(z_1)=a_{mz}(z_2)=g_0$ and at O_2 the levitation equilibrium is stable, whereas at O_1 it is unstable.

A levitation point is a point where the magnetic force exactly compensates Earth's gravity [$\mathbf{g}=\mathbf{0}$ in Eq. (2)]. The levitated state happens when a levitation point coincides with the center of the cell. In our apparatus the center of the cylindrical sample cell is located on the vertical coil axis (z axis) at point O of altitude z_0 [Fig. 2(a)] where the magnetic force reaches its maximum intensity. Therefore in the levitated state the magnetic acceleration exactly compensates Earth's gravity at point O only. Since in the vicinity of point O the vertical force is directed downward, the center of the

cell is an unstable equilibrium point on the vertical z axis and the modulus of the acceleration is a quadratic function of z along the vertical axis, which means that it varies quite slowly with z. The authors of Ref. [6] used a simple method to make a stable levitation equilibrium. In their apparatus, the sample was not placed at the altitude of the maximum of the magnetic force, but slightly higher [point O_2 of altitude z_2 in Fig. 2(b)]. The levitation state is attained at a slightly larger magnetic field intensity, but the equilibrium is stable. However, in this case, the acceleration along the z axis in the vicinity of the center of the cell is linear in z. Although the levitation is unstable in our apparatus, the inhomogeneities of the acceleration field along the z axis are reduced compared to the setup of Ref. [6]. In our cell the walls of the sample cell limit the motion of the fluid around the unstable equilibrium point O.

III. ANALYSIS OF THE SHAPE OF THE MENISCUS

A. Measuring the capillary length from the meniscus shape

When ℓ_C is much smaller than the horizontal extension of the sample cell (that is, the extension perpendicular to Earth's gravity), $\mathcal{B} \gg 1$ and the interface is flat except close to the walls, where its curvature scales with ℓ_C. It is straightforward to extract from the shape of the meniscus the value of the capillary length by using the fitting method described below. When ℓ_C is equal to or larger than the horizontal extension of the vessel, the interface is nearly spherical, and the determination of ℓ_C is much more difficult. In order to easily determine the capillary length, it is therefore preferable to keep the ratio between the capillary length and the horizontal extension of the vessel as small as possible ($\mathcal{B} \gg 1$). The lowest limit is given by the spatial resolution of the detection of the meniscus shape and the accuracy of the temperature control. Warren and Webb [13] used this method to deduce the interfacial tension from the capillary length measurements near the consolute point of near-critical cyclohexane-methanol mixtures under Earth's gravity. We inverted their method in order to deduce the effective acceleration from the capillary length measurements. We present in detail the model that justifies the method.

We assume a rectangular vessel of horizontal (perpendicular to gravity $\mathbf{g}_0$) dimensions L and e, containing a two-phase fluid system. A sketch of the shape of the interface is drawn in Fig. 3 together with the Cartesian coordinates which will be used in this section. Denoting by R_1 and R_2 the two principal curvature radii of the interface at point M of altitude z, the equilibrium shape of the gas-liquid interface for a constant acceleration g is determined by the balance of the pressures at the interface:

$$\frac{\sigma}{R_1}+\frac{\sigma}{R_2}-(\rho_L-\rho_V)gz=\text{const.} \tag{11}$$

In the Cartesian coordinates defined in Fig. 3 the principal curvature radii of the interface are defined as

$$R_x=\frac{[1+(\partial_x z)^2]^{3/2}}{\partial_{xx}z}, \quad R_y=\frac{[1+(\partial_y z)^2]^{3/2}}{\partial_{yy}z}, \tag{12}$$

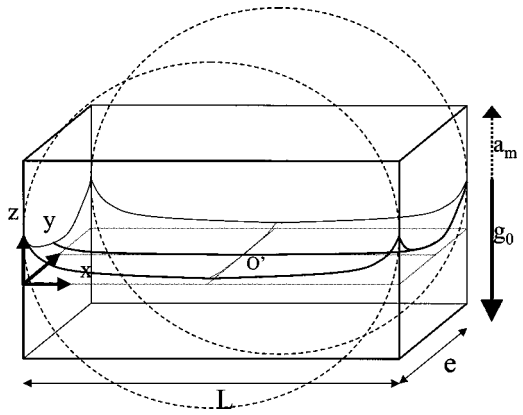

FIG. 3. Sketch of the shape of the interface and of the coordinates used in the model (the altitude $z=0$ corresponds to the lowest point of the gas-liquid interface). The vessel is assumed to be rectangular of horizontal dimensions L and e. The curved solid line in the center of the cell is the intersection of the interface with the plane $y=e/2$, i.e., the shape of the bottom of the meniscus which is observed in transmission and digitized (the curved dotted line is the intersection of the interface with the plane $x=L/2$). The shape of the experimental cylindrical vessel is superimposed on the shape of the rectangular vessel (dashed circles).

where ∂_m and ∂_{mm} are the first and second partial derivatives with respect to $m=\{x,y\}$, and $z(x,y)$ is the equation of the surface of the meniscus. For symmetry reasons the interface is flat at the center of the cell ($x=L/2$, $y=e/2$). If the capillary length is much smaller than e and L, it is meaningful to consider the curvature radii as infinite at the center ($\partial_{xx}z=\partial_{yy}z=0$). Assigning the altitude $z=0$ to the bottom of the meniscus (point O'), the constant in Eq. (11) is zero. Integrating Eq. (12) and using this boundary condition leads to the following equation of the surface of the meniscus:

$$\frac{z^2}{2\ell_C^2}=2-[1+(\partial_x z)^2]^{-1/2}-[1+(\partial_y z)^2]^{-1/2}. \tag{13}$$

The shape of the meniscus that is observed is the intersection of the interface with the plane $y=e/2$, in which $\partial_y z=0$. Writing Eq. (13) in this plane, one obtains a differential equation defining the shape of the meniscus at $y=e/2$:

$$\frac{z^2}{2\ell_C^2}=2-[1+(\partial_x z)^2]^{-1/2}. \tag{14}$$

The liquid completely wets the cell walls [14], implying that very near the wall the meniscus is parallel to the wall. But the influence of the complete wetting on the curvature of the interface is limited to the close vicinity of the wall (of the order of some nanometers). Farther from the solid wall, the shape of the meniscus does not depend on the wetting properties of the fluid, but only on the liquid-vapor equilibrium and gravity. This is why the shape of the meniscus is the same in a rectangular cell and in a cylindrical cell, excepting very close to the wall where, anyway, the wetting influence remains within the spatial resolution of the camera (10 μm) and cannot be detected. Integrating again as in Ref. [13], one gets the analytic expression of the shape of the meniscus at $y=e/2$

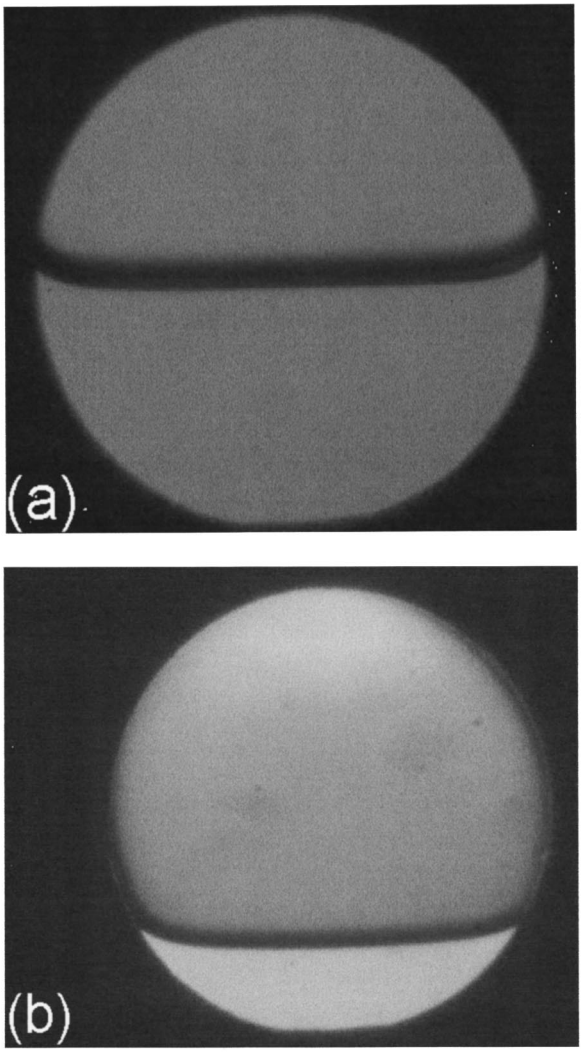

FIG. 4. Picture of the interface at (a) $T_C - T = 100\,\mathrm{mK}$, $g^* = 1$; (b) $T_C - T = 60\,\mathrm{mK}$, $g^* = 0.37$.

$$z(x) = z_{\max}\left[\exp\left(-\frac{x}{\ell_C}\right) + \exp\left(\frac{x-L}{\ell_C}\right)\right], \qquad (15)$$

where $z_{\max}$ is itself a function of ℓ_C. This solution is in fact the sum of two independent menisci in semi-infinite vessel.

In Fig. 4 two typical pictures of the interface at various temperatures and effective gravity levels g^* are shown. The dark stripe corresponds to the ascension of the liquid on the sapphire windows, which refracts the parallel light out of the field of view. Note that the low position of the meniscus in Fig. 4(b) is not due to a leak or an increase of the gas volume fraction but to the increase of the wetting layer thickness on the cell walls when the magnetic field is applied. This phenomenon is fully reversible when the magnetic field is removed. Due to the fact that our cell is not rectangular but cylindrical, its width (e in Fig. 3) is constant but its length (L in Fig. 3) depends on the shape of the meniscus because the walls are not vertical. In order to use Eq. (15) the actual length L is measured on each picture. The connection between the actual length of the interface and the model is shown in Fig. 3, where the shape of the cylindrical cell (dashed circles) is superimposed on the shape of the rectangular vessel of the model. The model described above is valid provided that the actual lengths of the interface L and e are large compared to the capillary length. For all the images analyzed the ratio between L and the measured capillary length is equal to 12.7 on average with a minimum of 6.0, whereas the ratio between e and the capillary length is equal to 9.2 on average with a minimum of 5.7, which ensures the validity of the approximations used in the model.

The shape of the meniscus at $y = e/2$ corresponds to the bottom of the dark stripe. This shape shown in Fig. 5 is determined from the image after correcting for an eventual tilt of the image due to a slight tilt of the camera, by numerically applying an intensity gradient operator to the digitized image along the vertical direction oriented from bottom to top of the image, and by extracting the curve of intensity maxima from the modified image. The altitude of the bottom of the meniscus shape is then shifted to zero. The length ℓ_C is deduced from the best fit of the meniscus shape using Eq. (15). The parameter $z_{\max}$ is the highest altitude reached by the meniscus on the cell walls. In the picture of Fig. 4(b) the ascension of the meniscus on the cell walls is not symmetric. This is due to a slight tilt of the camera, which is compensated before image analysis. The asymmetry of the detected meniscus shape visible in Figs. 5(a) and 5(b), ranging over one or two pixels, is due to defects of the walls or of the optics. Since Eq. (15) is the superposition of two independent shapes of meniscus minimizing the interfacial energy in a semi-infinite vessel, and sisnce the two exponential ascensions of the liquid are spatially well separated, the two shapes can be considered independently. When it occurs, such asymmetry is thus taken into account by fitting the profile with a slightly different formula:

$$z(x) = z_{\max,\mathrm{left}}\exp\left(-\frac{x}{\ell_C}\right) + z_{\max,\mathrm{right}}\exp\left(-\frac{x-L}{\ell_C}\right), \qquad (16)$$

where $z_{\max,\mathrm{left}}$ is the ascension height of the liquid at $x = 0$ and $z_{\max,\mathrm{right}}$ is the ascension height of the liquid at $x = L$.

B. Measuring the effective gravity from the capillary length

Taking into account the restricted domain of validity of the meniscus shape model, the accuracy of the temperature regulation, and the phenomenon of increased wetting under weak gravity, the measurements had to be performed in the temperature range $T_C - T = [12\,\mathrm{mK} - 500\,\mathrm{mK}]$, or $\tau = [5 \times 10^{-4} - 2 \times 10^{-2}]$ and for a reduced acceleration ranging from $g^* = 0.25$ to $g^* = 1$. In order to evaluate the homogeneity of the effective acceleration field, we have to check that: (i) the meniscus shape fits its theoretical shape in a homogeneous acceleration field according to Eq. (15) or Eq. (16) and (ii) the effective gravity deduced from the measured capillary length is compatible with the effective gravity deduced from the value of the electric current.

1. Meniscus shape fit

The fit is based on the minimization of the following χ^2 function, with ℓ_C as the only adjustable free parameter:

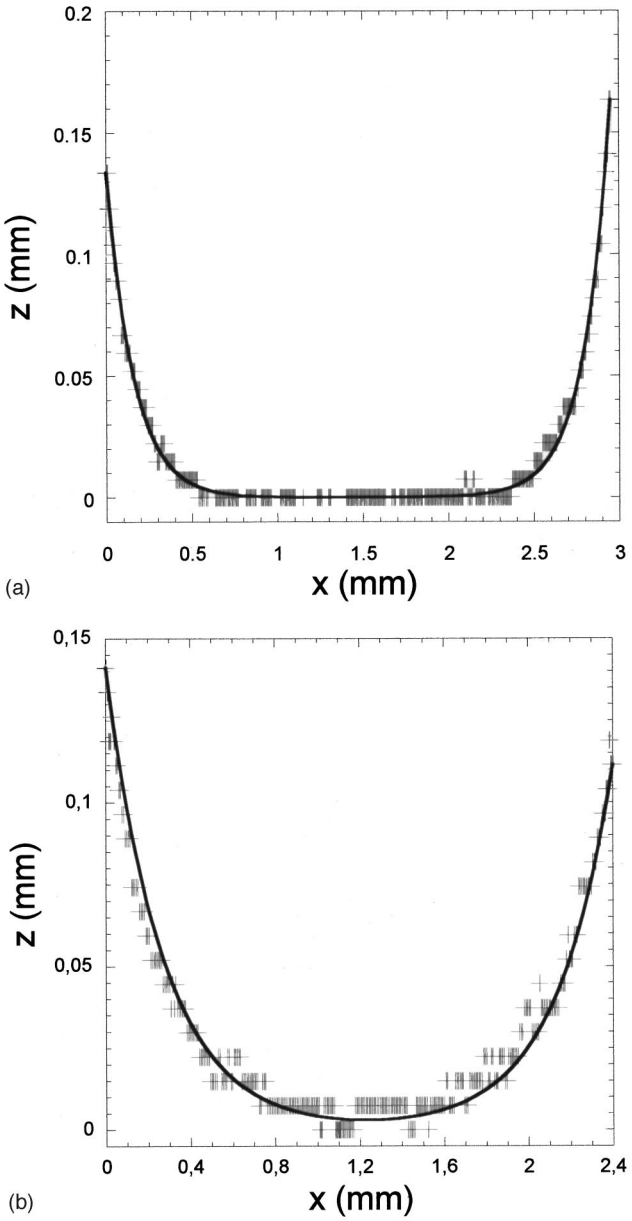

FIG. 5. Digitized shape of the meniscus at FWHM (+) together with the best fit (solid line) using Eq. (15) corresponding (a) to Fig. 4(a); (b) to Fig. 4(b). Note the different length scales on the x and z axes.

$$\chi^2=\sum_{i=1}^{N}[z_i-z(x_i)]^2, \tag{17}$$

where $(x_i,z_i)_{i=1,N}$ are the experimental digitized coordinates of the shape of the meniscus, and z is the fitting function of Eq. (15). The agreement between the best fit and the shape of the meniscus can be evaluated by computing Pearson's R coefficient:

$$R=\sqrt{1-\chi^2/\Sigma_{i=1}^{N}(z_i-\overline{z})^2}, \tag{18}$$

where $\overline{z}$ is the mean of $(z_i)_{i=1,N}$. The closer R is to unity, the better is the agreement between the best fit and the meniscus shape. For all the meniscus shapes analyzed in this study, R was always larger than 0.931 with a mean of 0.983, meaning

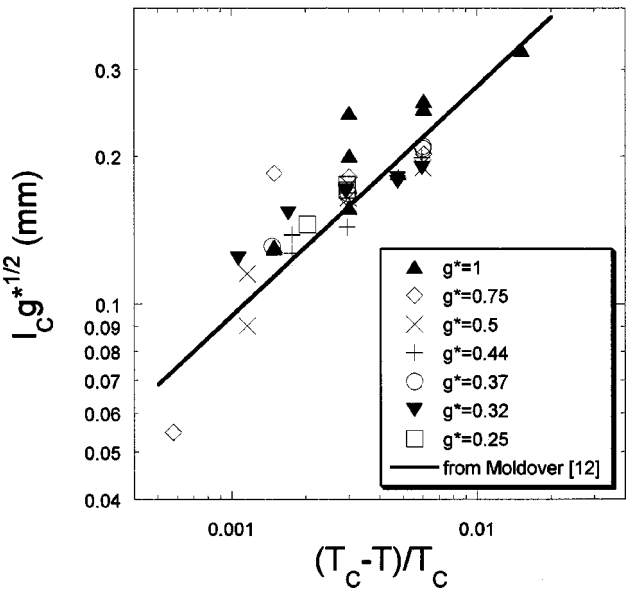

FIG. 6. The quantity $\ell_C g^{*1/2}$ as a function of the reduced distance to the critical temperature $(T_C-T)/T_C$ measured at various reduced gravity levels. ℓ_C is the capillary length determined from meniscus shape analysis and g^* is the effective acceleration reduced by Earth's gravity. The solid line is the power law of Eq. (9) for the capillary length using Moldover's data [12].

that the meniscus shape was very close to the shape of a meniscus in a homogeneous acceleration field. Figures 5(a) and 5(b) show two typical menisci with their best fits. Note that the agreement between the meniscus and its best fit does not exhibit any systematic distortion, showing that the acceleration field is indeed homogeneous, as assumed in the derivation of the fitting function.

2. Capillary length comparison

We now compare the capillary length measurements performed at $g^*\neq 1$ to the measurements at $g^*=1$ (in the absence of applied magnetic forces). According to the definition of the capillary length in Eq. (6), the quantity $\ell_C g^{*1/2}$ should be independent of g^* and should behave as the capillary length at $g^*=1$ according to the critical scaling law of Eq. (9). In Fig. 6 the quantity $\ell_C(g^*)^{1/2}$ is plotted as a function of τ together with the power law of Eq. (9), with the value $\ell_{C0}=2.39$ mm from Moldover [12] and the exponent 0.4675. Two remarks can be made.

First, the dispersion of the experimental data around the power law of Eq. (9) is the same at high g^* (where homogeneous Earth's gravity is dominant) as at low g^* (where magnetic forces are comparable to Earth's attraction). It follows that this dispersion is not due to inhomogeneities of the effective acceleration field.

Second, the data set is well represented by the power law with $\ell_{C0}=2.39$ mm, computed from the data of Moldover [12], who used the measurements by Blagoi and Pashkov [15]. Moreover, a power law fit with fixed exponent and ℓ_{C0} as free parameter gives $\ell_{C0}=2.47\pm0.06$ mm. Blagoi and Pashkov measured ℓ_{C0} in n-H_2 with critical parameters slightly different from the p-H_2 data. (To our knowledge there are no surface tension measurements reported near the critical point of p-H_2.) The relative difference between the n-

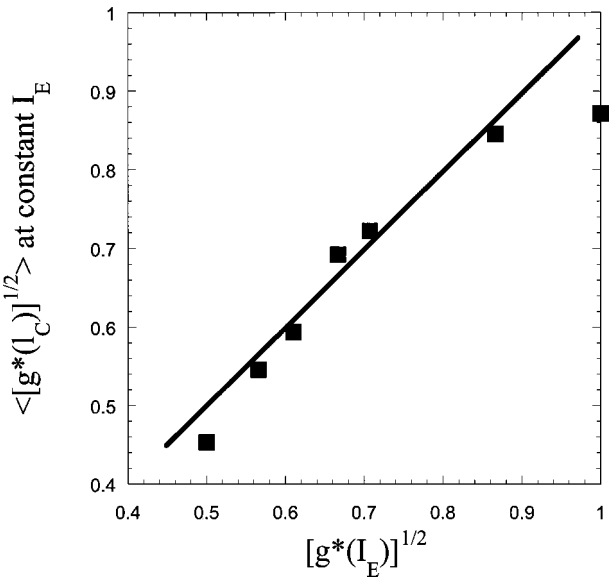

FIG. 7. Mean value of each data set $[g^*(\ell_C)]^{1/2}$ [defined in Eq. (19)] measured at given electric current I_E, corresponding to given value of the effective acceleration $g^*(I_E)$, as a function of $[g^*(I_E)]^{1/2}$ [defined in Eq. (10)].

and p-H_2 critical density (pressure) is less than 5‰ (5%). The surface tension of n-H_2 and p-H_2 should then differ by only a few percent. Blagoi and Pashkov worked far away from T_C, where weak crossover corrections to the asymptotic power law behavior of the surface tension might occur. The analysis of their data by Moldover [12] shows that the crossover behavior is weak for $\tau < 10^{-2}$. Taking into account all these considerations, our value of ℓ_{C0} can be considered as being in excellent agreement with the value of Moldover in Ref. [12].

Another test of self-consistency is to compare the values of $g^*(I_E)$ computed by using Eq. (10) with the values of g^* deduced from the capillary length measurements,

$$g^*(\ell_C) = \left(\frac{\ell_{C0} \tau^{0.4675}}{\ell_C} \right)^2 \tag{19}$$

using $\ell_{C0} = 2.39$ mm. Since the capillary length is sensitive to $g^{1/2}$, we plotted in Fig. 7 the mean value of each data set $[g^*(\ell_C)]^{1/2}$ measured at a given I_E [or equivalently at a given value of the effective acceleration $g^*(I_E)$] as a function of $[g^*(I_E)]^{1/2}$. The departure of the data from the ideal line of slope unity is more pronounced at high g^* than at low g^*, and thus is not due to inhomogeneities of the effective acceleration field. The dispersion of the data can be ascribed to the fluctuations of the temperature regulation.

As a partial conclusion, the above analysis of the meniscus shape shows that this magnetic levitation apparatus produces a satisfactory homogeneous acceleration field on the length scale of the sample cell.

IV. RESIDUAL ACCELERATION FIELD IN THE LEVITATION STATE

At exact compensation of Earth's gravity, the residual acceleration field can be determined by simple considerations on the magnetic field. In the following, natural cylindrical coordinates (r,z) centered along the vertical coil axis (z axis) are used. We assume that the levitation state happens at point O [Fig. 2(a)] and that the center of the sample cell coincides with O (of altitude z_0). In the absence of electric current, the static magnetic field satisfies $\mathrm{div}\,\mathbf{B} = 0$ and $\mathrm{curl}\,\mathbf{B} = \mathbf{0}$, which can be expressed as $\partial_r B_r(r,z) = -\frac{1}{2}\partial_z B_z(0,z)$ and $\partial_z B_r = \partial_r B_z$. Since the magnetic force exactly compensates the weight at the center of the cell, we write

$$\frac{|\chi|}{\rho \mu_0} B_z \partial_z B_z = g_0 . \tag{20}$$

Noting that $B_z(0,z_0) = b$, the magnetic field at the center of the cell, the characteristic length scale of the magnetic field gradient is

$$L_B = \frac{|\chi| b^2}{\rho \mu_0 g_0}, \tag{21}$$

with $b = 6.65$ T at weight compensation, $g_0 = 9.8\ \mathrm{m\,s^{-2}}$, $L_B = 89$ mm for our apparatus. Taking into account the fact that in our experiment the magnetic force is maximum at the center of the cell, that is, $\partial_z(B_z \partial_z B_z)(0,z_0) = 0$, the expansion of the magnetic field around the center of the cell restricted to the first nonzero order in r/L_B and $(z - z_0)/L_B$ leads to the following expressions for the components of the effective acceleration field $\mathbf{g}(r,z)$:

$$g_r(r,z) = -g_0 \frac{3r}{4L} + O(x^3, x = r, z - z_0), \tag{22}$$

$$g_z(r,z) = g_0 \left(\frac{r^2}{4L^2} - \frac{(z - z_0)^2}{4L^2} \right) + O(x^3, x = r, z - z_0). \tag{23}$$

The radial acceleration is thus directed toward the z axis, which means that the levitation equilibrium is stable to radial perturbations of small amplitude. Therefore the denser (liquid) phase should go to the middle of the cell, and the lighter (gas) phase should be rejected on the side walls of the cell [Fig. 2(b)]. The variations of the radial component of the acceleration in the vicinity of the center of the cell are much stronger than those of the axial component, since g_r is linear in r. In the levitation state, the residual gravity is roughly equal to the value of g_r for r equal to the radius of the cylindrical cell. For a 3 mm cell diameter, one gets $g_r \approx 0.13\ \mathrm{m\,s^{-2}} \approx 10^{-2} g_0$ at $r = 1.5$ mm, which is of the same order of magnitude as the residual gravity achieved during parabolic flights of planes. When Earth's gravity is only partially compensated ($g^* \neq 0$, $I_E < 63.1$ A) the acceleration inhomogeneity Δg^*, which is proportional to I_E^2, has a smaller amplitude than at $g^* = 0$ ($I_E = 63.1$ A). Consequently for $0 < g^* < 1$ the maximal amplitude of the acceleration inhomogeneity occurring in this apparatus is less than $10^{-2} g_0$.

The shape of the gas-liquid interface visible in Fig. 8 at 10 mK below the critical temperature in levitation in a cell of large diameter (10 mm) confirms the predictions about the residual acceleration field in levitation. The gas is rejected on the periphery of the cylindrical cell and the liquid is at its center, but part of the liquid is also located in the lower part

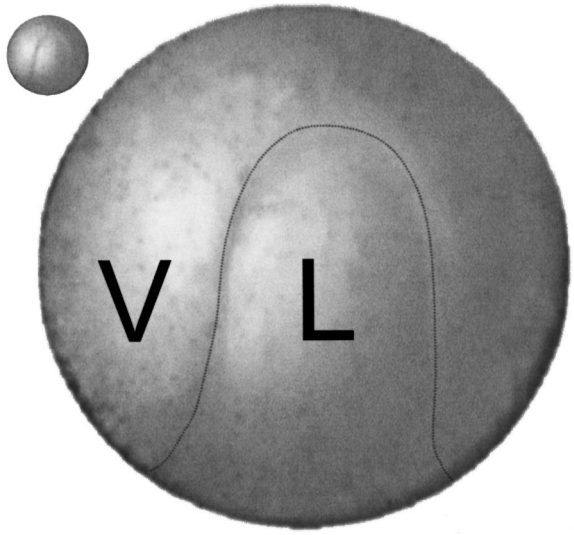

FIG. 8. Picture of the two-phase system at 10 mK below T_C in levitation state inside a cell of 10 mm diameter and 2 mm thickness. The central picture is an enlarged view of the picture on the left, where a dotted line underlines the interface. The levitation point is located in the center of the cell. Due to the residual radial acceleration field (which is linear in r and directed toward the center of the cell) existing around the levitation point, the liquid phase (L) is located in the center of the cell and the vapor phase (V) is rejected in the periphery of the cell, between a thin liquid wetting layer and the central liquid drop.

of the cell, due to the fact that the equilibrium is unstable at the cell center. The gas is also isolated from the cell wall by a liquid wetting layer (zero contact angle).

V. CONCLUDING REMARKS

Suppressing the effects of Earth's gravity by magnetic means is often cited as complementary to microgravity in space. The present experimental study shows that the situation is not so clear, as the magnetic compensation suffers from a number of difficulties and limitations. In order to investigate magnetic ''low gravity'' apparatus dedicated to the study of near-critical pure fluids, we used the vanishing properties of the capillary length of a two-phase system of H_2 at equilibrium as the critical point is approached. This is a very precise method to check the homogeneity of the effective acceleration field. Liquid and vapor phases of H_2 at coexistence were placed near the upper end of a vertical superconducting coil, in which the current was varied. For an effective acceleration ranging from 0.25 to 1 times Earth's gravity, the shape of the meniscus and the corresponding capillary length were compared to the theoretical shape of the meniscus under homogeneous gravity and the predicted value of the capillary length. It follows that no perceptible acceleration inhomogeneities were detected and that the main cause for the dispersion of the data can be attributed to the finite-level accuracy of our temperature control. The main difficulties arise from the influence of the magnetic field on the behavior of the thermometer and on the thermal properties of the materials (heat capacity and conductivity), which induce a drift of the regulated temperature as the electrical current is increased and a change of the best parameters of the regulation algorithm. Once these difficulties are overcome, this method can be applied to measurement of the interfacial tension closer to the critical point.

At exact compensation of the weight, when H_2 levitates, the main residual acceleration field is centripetal. In our smallest cell (3 mm diameter) its amplitude is of the order of $10^{-2}g_0$. It is worth noting that interesting thermal instabilities are likely to be observed in the very peculiar situation of such a radial field which resembles that inside the Earth's core.

ACKNOWLEDGMENTS

We thank J. Hegseth for useful discussion and for a critical reading of the manuscript. This work was supported by CNES Contract No. 793/CNES/97/6979.

[1] W. Braunbeck, Z. Phys. **112**, 735 (1939).
[2] E. Beaugnon and R. Tournier, J. Phys. III **1**, 1423 (1991).
[3] J. M. Valles, Jr., K. Lin, J. M. Denegre, and K. L. Mowry, Biophys. J. **73**, 1130 (1997).
[4] E. Beaugnon, D. Bourgault, D. Braithwaite, P. de Rango, R. Perrier de la Bathie, A. Sulpice, and R. Tournier, J. Phys. I **3**, 399 (1993).
[5] M. A. Weilert, D. L. Whithaker, H. J. Maris, and G. M. Seidel, Phys. Rev. Lett. **77**, 4840 (1996).
[6] M. A. Weilert, D. L. Whithaker, H. J. Maris, and G. M. Seidel, J. Low Temp. Phys. **106**, 101 (1997).
[7] D. L. Whithaker, M. A. Weilert, C. L. Vicente, H. J. Maris, and G. M. Seidel, J. Low Temp. Phys. **110**, 173 (1998).
[8] U. E. Israelson and M. Larson, in Proceedings of the 33rd Aerospace Sciences Meeting and Exhibit, Reno, 1995 [AIAA J. **95**, 272 (1995)].
[9] D. Beysens and Y. Garrabos, in *Proceedings of the 1st Symposium on the Utilization of the International Space Station, Darmstadt, 1995* (European Space Agency [Spec. Publ.] **ESA SP-385**, 647 (1996)).
[10] *Encyclopédie des Gaz*, edited by L'Air Liquide (Elsevier, Amsterdam, 1976), p. 915.
[11] J. V. Sengers and J. M. H. Levelt-Sengers, in *Progress in Liquid Physics*, edited by C. A. Croxton (Wiley, New York, 1978), p. 103.
[12] M. R. Moldover, Phys. Rev. A **31**, 1022 (1985).
[13] C. Warren and W. W. Webb, J. Chem. Phys. **50**, 3694 (1969).
[14] J. W. Cahn, J. Chem. Phys. **66**, 3667 (1977).
[15] Y. P. Blagoi and V. V. Pashkov, Zh. Eksp. Teor. Fiz. **49**, 1453 (1965) [Sov. Phys. JETP **22**, 999 (1966)].